Continuous Mesh Framework Part II: Validations and Applications

Adrien Loseille, Frédéric Alauzet

CONTINUOUS MESH FRAMEWORK PART II: VALIDATIONS AND APPLICATIONS

ADRIEN LOSEILLE* AND FRÉDÉRIC ALAUZET†

Abstract. This paper gives a numerical validation of the continuous mesh framework introduced in Part I [16]. We numerically show that the interpolation error can be evaluated analytically once analytical expressions of a mesh and a function are given. In particular, the strong duality between discrete and continuous views for the interpolation error is emphasized on 2D and 3D examples. In addition, we show the ability of this framework to predict the order of convergence, given a specific adaptive strategy defined by a sequence of continuous meshes.

The continuous mesh concept is then used to devise an adaptive strategy to control the $\mathbf{L}^p$ norm of the continuous interpolation error. Given the $\mathbf{L}^p$ norm of the continuous interpolation error, we derive the optimal continuous mesh minimizing this error. This exemplifies the potential of this framework as we use a calculus of variations that is not defined on the space of discrete meshes. Anisotropic adaptations on analytical functions correlate the optimal predicted theoretical order of convergence. The extension to solution of non-linear PDEs is also given. Comparisons with experiments show the efficiency and the accuracy of this approach.

Key words. Unstructured mesh, continuous mesh, Riemannian metric space, interpolation error, linear interpolate, anisotropic mesh adaptation, optimal interpolation error bound.

AMS subject classifications. 65D05, 65L50, 65N15, 65N50

Introduction. In this paper, we numerically validate the continuous mesh framework introduced in Part I [16]. Then, we use it to establish an optimal adaptive strategy to control the global linear interpolation error in $\mathbf{L}^p$ norm.

The main results of the continuous mesh framework described in Part I are the definitions of continuous elements, continuous meshes and the continuous linear interpolate, along with a point-wise estimate of the continuous linear interpolation error. A continuous mesh of a domain $\Omega \subset \mathbb{R}^3$ is a function $\mathbf{M} = (\mathcal{M}(\mathbf{x}))_{\mathbf{x}\in\mathbf{\Omega}}$ that associates with each point $\mathbf{x}$ of Ω a metric tensor $\mathcal{M}(\mathbf{x})$. As $\mathcal{M}(\mathbf{x})$ is a definite positive matrix, we use its spectral decomposition. We denote by $(\lambda_i)_{i=1,3}$ its eigenvalues along the eigen directions $(\mathbf{v}_i)_{i=1,3}$. The sizes prescribed by $\mathcal{M}$ are $(h_i)_{i=1,3} = (\lambda_i^{-2})_{i=1,3}$. According to Proposition 2.4 of Part I, the continuous mesh locally writes:

$$\mathcal{M}(\mathbf{x}) = d^{\frac{2}{3}}(\mathbf{x})\,\mathcal{R}(\mathbf{x}) \begin{bmatrix} r_1^{-\frac{2}{3}}(\mathbf{x}) & & \\ & r_2^{-\frac{2}{3}}(\mathbf{x}) & \\ & & r_3^{-\frac{2}{3}}(\mathbf{x}) \end{bmatrix} {}^t\mathcal{R}(\mathbf{x}),$$

where

- the density d is equal to: $d = (h_1\,h_2\,h_3)^{-1} = (\lambda_1\,\lambda_2\,\lambda_3)^{\frac{1}{2}}$,
- the anisotropic quotients r_i are equal to: $r_i = h_i^3\,(h_1\,h_2\,h_3)^{-1}$.

The point-wise continuous interpolation error of a function u on $\mathbf{M}$ is given by:

$$\begin{aligned} \forall \mathbf{a} \in \Omega\,, \quad |u - \pi_{\mathcal{M}} u|(\mathbf{a}) &= \frac{1}{10}\,\mathrm{trace}\big(\mathcal{M}(\mathbf{a})^{-\frac{1}{2}}\,|H_u(\mathbf{a})|\,\mathcal{M}(\mathbf{a})^{-\frac{1}{2}}\big) \\ &= \frac{1}{10}\,\Big(\,d(\mathbf{a})^{-\frac{2}{3}} \sum_{i=1}^{3} r_i(\mathbf{a})^{\frac{2}{3}}\;{}^t\mathbf{v}_i(\mathbf{a})\,|H_u(\mathbf{a})|\,\mathbf{v}_i(\mathbf{a})\,\Big), \end{aligned}$$

*INRIA Rocquencourt, Gamma team, France, (Adrien.Loseille@inria.fr).
†INRIA Rocquencourt, Gamma team, France, (Frederic.Alauzet@inria.fr).

where $\pi_{\mathcal{M}}$ is the continuous linear interpolate and H_u is the Hessian of u, see Corollary 3.4 in Part I.

The scope of this paper is first to numerically validate the previous estimate. It consists in verifying that the computation of the discrete interpolation error on a unit mesh $\mathcal{H}$ with respect to $\mathbf{M}$:

$$\|u - \Pi_h u\|_{\mathbf{L}^1(\Omega_h)} = \sum_{K \in \mathcal{H}} \|u - \Pi_h u\|_{\mathbf{L}^1(K)}, \tag{D}$$

is an approximation of the continuous interpolation error calculated on $\mathbf{M}$:

$$\|u - \pi_{\mathcal{M}} u\|_{\mathbf{L}^1(\Omega)} = \int_{\Omega} |u - \pi_{\mathcal{M}} u|(\mathbf{x})\, \mathrm{d}\mathbf{x}. \tag{C}$$

If Propositions 2.3, 2.4 and Theorems 3.2, 3.3 defined in [16] show a strong duality between the continuous and the discrete views for the linear interpolation error, a numerical validation is necessary to fully assess the continuous mesh concept. In particular, Theorems 3.2 and 3.3 of Part I use a second order Taylor expansion of the considered function. Exact relations between continuous and discrete interpolation errors are only valid for quadratic functions. Furthermore, it is interesting to measure how the discrete error (D) approximates the continuous one (C) on the whole computational domain as the continuous-discrete equivalence formula, given by Theorem 3.3 in Part I, is local. Consequently, the asymptotic behavior of the continuous interpolation error needs to be verified on non-linear examples. In addition, we demonstrate that, from the analytic expression of the global continuous interpolation error given by (C), the order of convergence of the error is automatically predicted for the considered sequence of continuous meshes with an increasing complexity. The sequence of continuous meshes can be embedded according to Definition 2.5 in [16] or can be in-homogeneous. In the latter case, the increasing factor of the density depends on the directions of anisotropy.

This study also shows that the use of a discrete support is no more mandatory to compute the interpolation error, it can be derived analytically. Nevertheless, if the calculus cannot be performed (for instance when dealing with real-life applications), only a background mesh that supports a discrete representation of the continuous mesh is needed to evaluate the error. Moreover, we illustrate that the interpolation error can be calculated for any function provided on any continuous mesh. No specific requirement in the computation of the linear interpolation error is made. For instance, there is absolutely no assumption on $\mathbf{M}$, neither on its density distribution, nor on its orientation.

Previous considerations are relative to the prediction of the interpolation error both in magnitude and rate of convergence. A legitimate application of this work is then to seek for the optimal continuous mesh minimizing the interpolation error for a given function. This problem is usually referred to as mesh adaptation. In its more general form, the problem of mesh adaptation consists in finding the mesh $\mathcal{H}$ of a domain Ω that minimizes a given error for a given function u. For the sake of simplicity, we consider here the linear interpolation error $u - \Pi_h u$ controlled in $\mathbf{L}^p$ norm. Note that considering other norms also works [14]. The problem is thus stated in an *a priori* way:

$$\text{Find } \mathcal{H}_{opt} \text{ having } N \text{ nodes such that } E(\mathcal{H}_{opt}) = \min_{\mathcal{H}} \|u - \Pi_h u\|_{\mathbf{L}^p(\Omega_h)}. \tag{P}$$

(P) is a global combinatorial problem which turns out to be intractable practically. Indeed, this would require the simultaneous optimization of both the mesh topology and the vertices location, a problem which cannot be considered. Consequently, simpler problems are considered to approximate the solution. A common simplification is to perform a local analysis of the error instead of considering the global problem. A first set of methods consists in deriving the optimal element shape [5]. A second set consists in deriving a local bound of the interpolation error. This bound is then transformed into a metric-based estimate [9, 10, 14, 18]. Direct minimization of the error can also be considered by using directly the interpolation error as a cost function in the mesh generator [15]. All these strategies have in common the resolution of a local problem as they act in the vicinity of an element. Consequently, such error minimizations are equivalent to a steepest descent algorithm that converges only to a local minimum with poor convergence properties. This drawback arises because we consider directly the minimization on a discrete mesh.

We propose in this paper to address the resolution of (P) in a continuous setting. Consequently, (P) is recast as a continuous optimization problem where the discrete interpolation error is replaced by the continuous one. Contrary to discrete-based study, the continuous formulation succeeds in solving globally the optimal interpolation error problem by using powerful mathematical tools such as calculus of variations. Unicity of the solution along with an optimal bound of the interpolation error are deduced from this analysis.

To assess the anisotropic mesh adaptation process along with its efficiency and accuracy, we apply it to analytic functions and to numerical solutions of PDEs.

Overview. In Section 1, numerical experiments are carried out to validate the continuous estimate of the interpolation error. They emphasize the possibility to compute, for a given analytic function and a given continuous mesh, the continuous interpolation error without any discrete supports. The correlation between continuous and discrete estimations of the interpolation error is shown. Then, in Section 2, the problem of finding the optimal continuous mesh minimizing the interpolation error in $\mathbf{L}^p$ norm is solved by a calculus of variations. An optimal bound of the error is also given. Finally, in Section 3, the mesh adaptation procedure based on the control of the interpolation error in $\mathbf{L}^p$ norm is presented. Several analytical examples on smooth and low regularity functions illustrate the efficiency of the proposed method. The approach is also validated in the context of solutions of PDEs by comparing numerical adaptive solutions with experimental values.

1. Numerical validation of the continuous interpolation error model. Using the continuous mesh framework introduced in [16], the continuous linear interpolation error in $\mathbf{L}^1$ norm can be analytically computed for any analytic function u given on any continuous mesh $\mathbf{M} = (\mathcal{M}(\mathbf{x}))_{\mathbf{x}\in\Omega}$ of a domain Ω. This calculus does not require any discrete support, e.g. any mesh. In this section, this is emphasized on several examples in 2D and 3D. To validate the approach, each calculated continuous interpolation error is compared to the discrete interpolation error computed on a unit mesh with respect to the continuous one.

1.1. Continuous interpolation error calculation.

Embedded continuous meshes. We consider the set of continuous embedded meshes $\mathbf{M}_1(\alpha) = (\mathcal{M}_{1,\alpha}(\mathbf{x}))_{\mathbf{x}\in\Omega_1}$ defined on square domain $\Omega_1 = [0,1]\times[0,1]$ and given by:

$$\mathcal{M}_{1,\alpha}(x,y) = \alpha \begin{bmatrix} h_1^{-2}(x,y) & 0 \\ 0 & h_2^{-2}(x,y) \end{bmatrix},$$

where $h_1(x,y) = 0.1(x+1)+0.05(x-1)$ and $h_2(x,y) = 0.2$. The parameter α is used to control the level of accuracy of the mesh. The continuous mesh $\mathbf{M}_1(\alpha)$ becomes coarser when α decreases but anisotropic quotients and orientations remain constant. This trend is given by the computation of the complexity $\mathcal{C}(\mathbf{M}_1(\alpha))$:

$$\mathcal{C}(\mathbf{M}_1(\alpha)) = N(\alpha) = \iint_{\Omega_1} \frac{1}{h_1 h_2}(x,y)\,\mathrm{d}x\mathrm{d}y = \frac{200}{3}\ln(2)\alpha.$$

The parameter α (or N) defines embedded continuous meshes accordingly to Definition 2.5 of [16]. The continuous interpolation error on $\mathbf{M}_1(\alpha)$ is computed for two analytical functions u_1 and u_2:

- u_1 is a quadratic function given by: $u_1(x,y) = 6x^2 + 2xy + 4y^2$,
- u_2 is a non quadratic function given by: $u_2(x,y) = \mathrm{e}^{(2x^2+y)}$.

As regards function u_1, the point-wise continuous interpolation error on $\mathbf{M}_1(\alpha)$ is:

$$\begin{aligned}(u_1 - \pi_{\mathcal{M}_{1,\alpha}} u_1)(x,y) &= \frac{1}{8}\,\mathrm{trace}\left(\mathcal{M}_{1,\alpha}^{-\frac{1}{2}}(x,y)\,|H_{u_1}(x,y)|\,\mathcal{M}_{1,\alpha}^{-\frac{1}{2}}(x,y)\right)\\ &= \frac{3\,(0.15x+0.05)^2}{2\,\alpha} + \frac{0.04}{\alpha}\\ &= \frac{27\,x^2+18\,x+35}{800\,\alpha}.\end{aligned}$$

The previous expression is then integrated over Ω_1:

$$\iint_{\Omega_1} |u_1 - \pi_{\mathcal{M}_{1,\alpha}} u_1|(x,y)\,\mathrm{d}x\mathrm{d}y = \frac{53}{800\,\alpha} = \frac{53}{12}\frac{\ln(2)}{N(\alpha)}.$$

For function u_2, the point-wise continuous interpolation error on $\mathbf{M}(\alpha)$ is:

$$\begin{aligned}(u_2 - \pi_{\mathcal{M}_{1,\alpha}} u_2)(x,y) &= \frac{1}{8}\,\mathrm{trace}\left(\mathcal{M}_{1,\alpha}^{-\frac{1}{2}}(x,y)\,|H_{u_2}(x,y)|\,\mathcal{M}_{1,\alpha}^{-\frac{1}{2}}(x,y)\right)\\ &= \frac{e^{4x^2+y}}{8\,\alpha}\left((0.15x+0.05)^2\,(4+16x^2)+0.05\right).\end{aligned}$$

By a direct integration over Ω_1, it comes:

$$\iint_{\Omega_1} |u_2 - \pi_{\mathcal{M}_{1,\alpha}} u_2|(x,y)\,\mathrm{d}x\mathrm{d}y \approx \frac{0.2050950191}{\alpha} \approx \frac{13.673\,\ln(2)}{N(\alpha)}.$$

Some remarks can be made before comparing the continuous evaluation of interpolation error to the discrete one, this will be done in the next section. According to the previous examples, if given a continuous mesh $\mathbf{M}(\alpha)$ of complexity N and a smooth function u, the continuous interpolation for u on $\mathbf{M}(\alpha)$ writes in a generic way:

$$\|u - \pi_{\mathcal{M}} u\|_{\mathbf{L}^1(\Omega_1)} = \frac{C_u}{N(\alpha)},$$

where C_u depends on u and $N(\alpha)$ is the complexity of $\mathbf{M}(\alpha)$. The previous expression gives a quantitative information on the order of convergence of the interpolation error on a sequence of continuous embedded meshes issued from $\mathbf{M}(1)$. Indeed, a simple analogy with uniform meshes leads to $N(\alpha) = O(h^{-2}(\alpha))$, so that:

$$\|u - \pi_{\mathcal{M}} u\|_{\mathbf{L}^1(\Omega_1)} = C_u \, h^2(\alpha).$$

Consequently, the continuous interpolation error model predicts an order of convergence of two on a sequence of embedded continuous meshes. From the discrete view, it is well known that a uniform refinement leads to a second order of convergence for the linear interpolation error with respect to a smooth function. This fact is also given by the continuous analysis. With this framework, the prediction of the rate of convergence is generalized to anisotropic meshes thank to the use of the continuous complexity. Indeed, a unique real parameter h as used classically [4] is no more sufficient to take into account anisotropic features for a sequence of meshes.

Non-embedded continuous mesh. Now, let us give a more complex example in order to demonstrate the ability of the continuous mesh model to predict the order of convergence. In this example, a discrete study of the prediction of the interpolation error is impossible whereas a clear convergence order is exhibited with the continuous mesh model. We consider the following set of continuous meshes $\mathbf{M}_2(\alpha) = (\mathcal{M}_{2,\alpha}(\mathbf{x}))_{\mathbf{x}\in\Omega_2}$ defined on square domain $\Omega_2 = [0.5, 1] \times [0.5, 1]$ and given by:

$$\mathcal{M}_{2,\alpha}(x,y) = F(x,y) \begin{bmatrix} \alpha^2 \, h_1^{-2}(x,y) & 0 \\ 0 & \alpha \, h_2^{-2}(x,y) \end{bmatrix} {}^t F(x,y),$$

$$\text{where} \qquad F(x,y) = \frac{1}{\sqrt{x^2+y^2}} \begin{bmatrix} x & -y \\ y & x \end{bmatrix},$$

$$\text{and} \quad h_1^{-2}(x,y) = 4(x^2+y^2) \quad \text{and} \quad h_2(x,y)^{-2} = \frac{1}{2\sqrt{x^2+y^2}}.$$

Note that this set is no more embedded accordingly to Definition 2.5 given in [16]. On the contrary, the continuous meshes are rather non uniformly embedded as one size is scaled by $1/\alpha$ and the other one is scaled by $1/\sqrt{\alpha}$. The equivalent discrete refinement process is no more homogeneous, *i.e.,* the factor of division of each edge while increasing α depends on the edge coordinates. Consequently, the order of convergence seems unpredictable *a priori* contrary to the embedded case. However, we show that we are able to predict the asymptotic convergence order of the continuous interpolation error for the set spanned by $\mathbf{M}_2(\alpha)$ by using the continuous analysis. The complexity of $\mathbf{M}_2(\alpha)$ is given by:

$$\mathcal{C}(\mathbf{M}_2(\alpha)) = N(\alpha) = \iint_{\Omega_2} \frac{1}{h_1 h_2}(x,y) \, \mathrm{d}x\mathrm{d}y \approx 0.364 \, \alpha^{\frac{3}{2}}.$$

We consider the interpolation error of the quadratic function u_3:

$$u_3(x,y) = x^2 + y^2.$$

The point-wise continuous interpolation error on $\mathbf{M}_2(\alpha)$ is given by:

$$\begin{aligned} (u_3 - \pi_{\mathcal{M}_{2,\alpha}} u_3)(x,y) &= \frac{1}{8} \operatorname{trace}\left(\mathcal{M}_{2,\alpha}^{-\frac{1}{2}}(x,y) \, |H_{u_3}(x,y)| \, \mathcal{M}_{2,\alpha}^{-\frac{1}{2}}(x,y) \right) \\ &= \frac{1}{16\,(x^2+y^2)\,\alpha^2} + \frac{\sqrt{x^2+y^2}}{2\,\alpha}. \end{aligned}$$

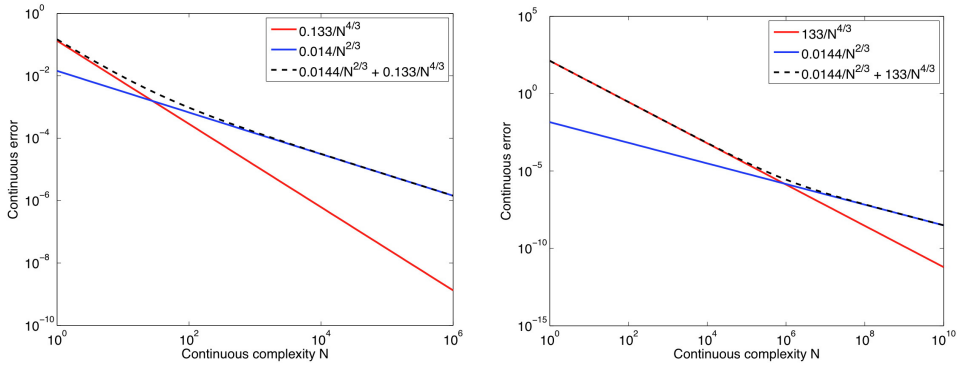

FIG. 1.1. *Left, convergence history obtained for the function u_3 on the set of inhomogeneous continuous meshes spans by $\mathbf{M}_2(\alpha)$ defined on Ω_2. Right, convergence history for the error function of Remark 1. In that specific case, the coefficients involved in the error expression lead to observe $O(N^{-\frac{4}{3}})$ as predominant term in the reachable range of complexity $[1, 10^6]$ whereas the asymptotic convergence order is $O(N^{-\frac{2}{3}})$.*

The previous expression is then integrated over Ω_2, it results:

$$\iint_{\Omega_2} |u_3 - \pi_{\mathcal{M}_{2,\alpha}} u_3|(x,y)\,\mathrm{d}x\mathrm{d}y \quad = \quad \frac{0.133}{N(\alpha)^{\frac{4}{3}}} + \frac{0.014}{N(\alpha)^{\frac{2}{3}}}.$$

The inhomogeneity in the scaling of the sizes leads to two terms with different order of convergence: $\frac{8}{3}$ and $\frac{4}{3}$ for the first and the second terms, respectively. Consequently, the asymptotic order of convergence for the continuous interpolation error of u_3 on $\mathbf{M}_2(\alpha)$ is only $O(N^{-\frac{2}{3}})$ leading to a convergence order of $\frac{4}{3} \approx 1.33$. This is less than the second order reached on the previous set of meshes defined by $\mathbf{M}_1(\alpha)$. Indeed, for a sufficiently large value of N, the term of order $O(N^{-\frac{4}{3}})$ becomes negligible with respect to the low order term $O(N^{-\frac{2}{3}})$. However, this approximation is only true asymptotically. Practically, the complexity allowing this simplification depends on the constant 0.014 and 0.133. According to Figure 1.1 (left), as soon as the complexity becomes greater than 1000, the asymptotic order of convergence is fully represented by $\frac{0.014}{N(\alpha)^{\frac{2}{3}}}$. Note that this value is reachable in practice on discrete meshes.

REMARK 1. *Depending on the constants involved in the estimation of the order of convergence, a convergence order different from the asymptotic one can be observed. If we suppose that the error for a function u on $\mathbf{M}_2(\alpha)$ now writes:*

$$\iint_{\Omega_2} |u - \pi_{\mathcal{M}_{2,\alpha}} u|(x,y)\,dx\,dy \quad = \quad \frac{133}{N(\alpha)^{\frac{4}{3}}} + \frac{0.014}{N(\alpha)^{\frac{2}{3}}}.$$

Then, the asymptotic complexity such that the term of order $\frac{4}{3}$ becomes negligible is difficult to reach in practice with discrete meshes (greater than 10^6), see Figure 1.1 (right). Consequently, the observed order of convergence for acceptable complexities ($\mathcal{C}(\mathbf{M}_2(\alpha)) \in [1, 10^6]$) is of the order of $O(N^{-\frac{4}{3}})$. This example shows that predicting both the order of convergence and the magnitude of the constants is crucial to get a reliable asymptotic prediction of the interpolation error.

In the next section, the analytic evaluation of the constant C_u along with the convergence order are compared to discrete estimations obtained by generating unit discrete meshes with respect to $\mathbf{M}_1(\alpha)$ and $\mathbf{M}_2(\alpha)$ for different values of α.

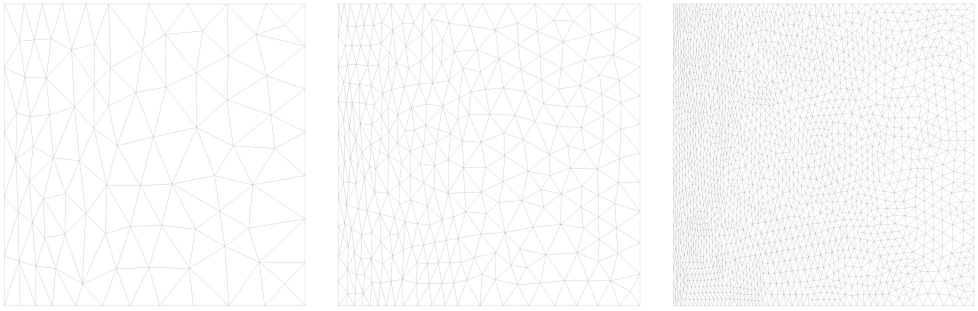

FIG. 1.2. *Unit meshes* $\{\mathcal{H}_{1,\alpha}\}_\alpha$ *with respect to* $\{\mathbf{M}_1(\alpha)\}_\alpha$ *on* Ω_1 *for* $\alpha = \{1, 8, 32\}$ *from left to right.*

1.2. Comparison with discrete interpolation error computation.

Unit meshes. To validate the previous continuous evaluation of the interpolation error, a series of discrete unit meshes with respect to $\mathbf{M}_1(\alpha) = (\mathcal{M}_{1,\alpha}(\mathbf{x}))_{\mathbf{x}\in\Omega_1}$ is generated. These meshes are considered for $\alpha = \{1, 2, 4, 8, 16, 32\}$. We denote by $\{\mathcal{H}_{1,\alpha}\}_{\alpha\in[1...32]}$ this sequence of discrete meshes. They have been generated using `Yams` [11]. Figure 1.2 depicts all these meshes. Histograms reporting for each mesh the length of its edges and the quality of its elements are given in Table 1.1. These histograms point out the gap between the generated unit meshes and a perfect unit mesh. We notice that an almost perfect quality is reached for each mesh and that more than 80% of the length of edges lie in the range $[\frac{\sqrt{2}}{2}, \sqrt{2}]$ as soon as $\alpha \geq 4$. Unit meshes sequence $\{\mathcal{H}_{2,\alpha}\}_{\alpha\in[16...512]}$ with respect to $\mathbf{M}_2(\alpha)$ are depicted in Figure 1.3. Similar conclusions arise.

Complexity vs. number of vertices. We first study the correlation between the discrete number of vertices N_v and the continuous complexity N. This preliminary study is necessary in the continuous discrete comparison. Indeed, the continuous interpolation error estimate involves the continuous complexity whereas the discrete number of vertices is used in the discrete error computation. As regards the sequence of discrete meshes $\{\mathcal{H}_{1,\alpha}\}_\alpha$ with respect to $\{\mathbf{M}_1(\alpha)\}_\alpha$, the discrete number of nodes N_v is plotted as a function of the complexity N in Figure 1.4 (top right). This function is linear and the slope evaluated numerically gives:

$$\forall \mathcal{H}_\alpha\,, \quad N_v(\alpha) = 1.54\, N(\alpha).$$

Note that this constant handles the discrepancy between the perfect unit mesh and the generated constrained discrete mesh with respect to the continuous one. Constraints arise from the domain boundary, the used mesh generator and the smoothness of the continuous mesh. This constant is in the theoretical framework equal to 2, see Theorem 3.3 in [16]. When the constant is equal to 2, it ensures the following equality between discrete and continuous errors:

$$\frac{C_u}{N} = 2\frac{C_u}{N_v}.$$

In the case of the set of inhomogeneous continuous meshes defined by $\mathbf{M}_2(\alpha)$, the constant is equal to 3.37.

Discrete interpolation error. The discrete interpolation error of a function u on a

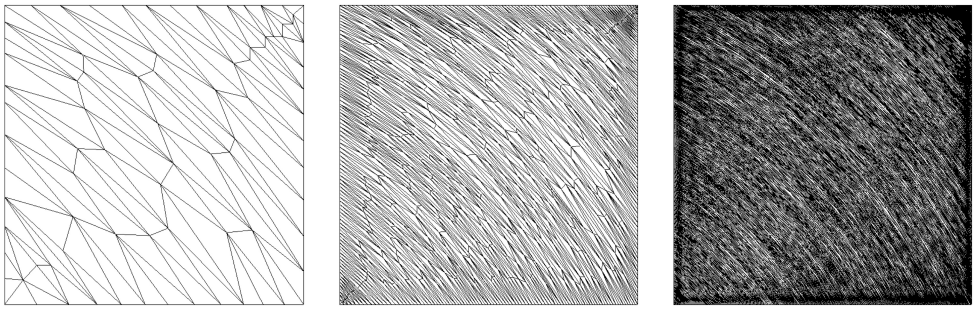

FIG. 1.3. *Unit meshes* $\{\mathcal{H}_{2,\alpha}\}_\alpha$ *with respect to* $\{\mathbf{M}_2(\alpha)\}_\alpha$ *on* Ω_2 *for* $\alpha = \{16, 128, 512\}$ *from left to right.*

mesh $\mathcal{H}_\alpha$ reads:

$$\|u - \Pi_h u\|_{\mathbf{L}^1(\mathcal{H}_\alpha)} = \sum_{K \in \mathcal{H}_\alpha} \|u - \Pi_h u\|_{\mathbf{L}^1(K)},$$

where K stands for an element of $\mathcal{H}_\alpha$. The element-wise interpolation error $\|u - \Pi_h u\|_{\mathbf{L}^1(K)}$ is computed by means of a 5-order Gauss quadrature numerical integration. The discrete interpolation error is compared to the continuous one by considering N_v instead of N in the continuous estimates. Figure 1.4 plots discrete and continuous interpolation errors for functions u_1 and u_2 on $\mathbf{M}_1(\alpha)$, and for function u_3 on $\mathbf{M}_2(\alpha)$. An excellent correlation is obtained between the continuous and the discrete evaluations. The slight differences between the continuous and the discrete expressions come from the practical difficulty to generate a perfect unit mesh. Indeed, mesh generators generate unit meshes in the sense of Definition 2.7 defined in [16]. It implies that elements are quasi-unit. In consequence, most of the length of edges lie in the range $[\frac{\sqrt{2}}{2}, \sqrt{2}]$. Bounds of the interpolation error can be deduced from this tolerance. For every function u and for every continuous mesh, we have :

$$\|u - \pi_{\mathcal{M}_{min}} u\|_{\mathbf{L}^1} \leq \|u - \pi_{\mathcal{M}} u\|_{\mathbf{L}^1} \leq \|u - \pi_{\mathcal{M}_{max}} u\|_{\mathbf{L}^1},$$

where $\mathcal{M}_{min} = 2\,\mathcal{M}$ and $\mathcal{M}_{max} = \frac{1}{2}\,\mathcal{M}$. Unit meshes composed of edges with a

$0.20 < L < 0.50$	5	1.94 %	$0.20 < L < 0.50$	1	0.19 %	$0.20 < L < 0.50$	6	0.71 %
$0.50 < L < 0.71$	53	20.54 %	$0.50 < L < 0.71$	130	25.15 %	$0.50 < L < 0.71$	82	9.69 %
$0.71 < L < 0.90$	116	44.96 %	$0.71 < L < 0.90$	204	39.46 %	$0.71 < L < 0.90$	352	41.61 %
$0.90 < L < 1.11$	68	26.36 %	$0.90 < L < 1.11$	133	25.73 %	$0.90 < L < 1.11$	279	32.98 %
$1.11 < L < 1.41$	16	6.20 %	$1.11 < L < 1.41$	49	9.48 %	$1.11 < L < 1.41$	127	15.01 %
$1 < Q < 2$	160	99.38 %	$1 < Q < 2$	328	99.39 %	$1 < Q < 2$	541	99.27 %
$2 < Q < 3$	1	0.62 %	$2 < Q < 3$	2	0.61 %	$2 < Q < 3$	4	0.73 %
$\mathcal{H}_{1,1}$			$\mathcal{H}_{1,2}$			$\mathcal{H}_{1,4}$		
			$0.20 < L < 0.50$	9	0.28 %	$0.20 < L < 0.50$	8	0.12 %
$0.50 < L < 0.71$	281	16.6 %	$0.50 < L < 0.71$	276	8.44 %	$0.50 < L < 0.71$	905	13.69 %
$0.71 < L < 0.90$	564	33.31 %	$0.71 < L < 0.90$	1436	43.89 %	$0.71 < L < 0.90$	2491	37.67 %
$0.90 < L < 1.11$	542	32.01 %	$0.90 < L < 1.11$	1071	32.73 %	$0.90 < L < 1.11$	2081	31.47 %
$1.11 < L < 1.41$	306	18.07 %	$1.11 < L < 1.41$	480	14.67 %	$1.11 < L < 1.41$	1127	17.04 %
$1 < Q < 2$	328	99.18 %	$1 < Q < 2$	328	99.77 %	$1 < Q < 2$	328	99.70 %
$2 < Q < 3$	2	0.82 %	$2 < Q < 3$	2	0.23 %	$2 < Q < 3$	2	0.30 %
$\mathcal{H}_{1,8}$			$\mathcal{H}_{1,16}$			$\mathcal{H}_{1,32}$		

TABLE 1.1

Quality $1/Q_{\mathcal{M}_1}$ *and length of the edges for the unit meshes* $\{\mathcal{H}_{1,\alpha}\}_\alpha$ *with respect to* $\{\mathbf{M}_1(\alpha)\}_\alpha$ *in 2D for* $\alpha = \{1, 2, 4, 6, 8, 16, 32\}$.

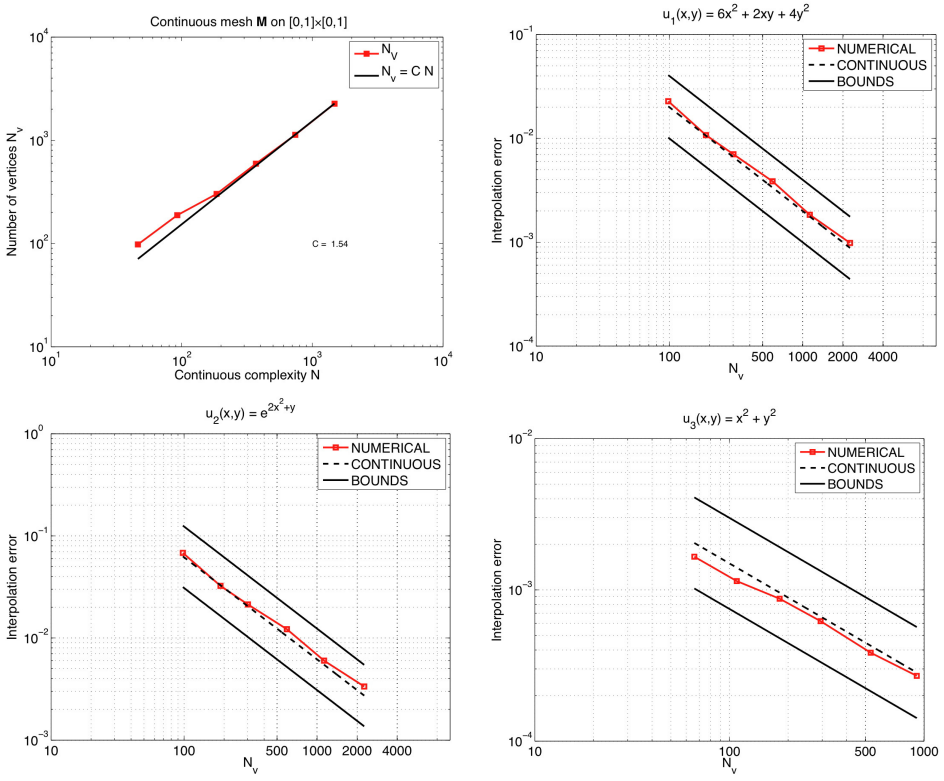

FIG. 1.4. *Top left, comparison between the continuous mesh complexity and the number of vertices for a sequence of unit meshes* $\{\mathcal{H}_{1,\alpha}\}_\alpha$ *with respect to* $\{\mathbf{M}_1(\alpha)\}_\alpha$. *Top right and bottom, comparison between continuous interpolation error* $\|u-\pi_{\mathcal{M}}u\|_{\mathbf{L}^1(\Omega)}$ *and discrete interpolation error* $\|u-\Pi_h u\|_{\mathbf{L}^1(\Omega_h)}$ *for function* u_1 *(top right),* u_2 *(bottom left) on* $\mathbf{M}_1(\alpha)$ *and* u_3 *(bottom right) on* $\mathbf{M}_2(\alpha)$. *Black plain lines represent continuous interpolation errors when considering* $\mathcal{M}_{max}$ *and* $\mathcal{M}_{min}$.

length lying in the acceptable range will verify:

$$\frac{1}{2}\|u-\pi_{\mathcal{M}}u\|_{\mathbf{L}^1} \leq \|u-\Pi_h u\|_{\mathbf{L}^1} \leq 2\|u-\pi_{\mathcal{M}}u\|_{\mathbf{L}^1}.$$

These bounds are plotted in Figure 1.4. Note that previous bounds impact only the constant evaluation C_u and not the order of convergence of the interpolation error.

1.3. 3D validation.

An analytical example. We first consider the set of 3D embedded continuous meshes $\mathbf{M}_3(\alpha) = (\mathcal{M}_{3,\alpha}(\mathbf{x}))_{\mathbf{x}\in\Omega_3}$ defined on the domain $\Omega_3 = [0,1]\times[0,1]\times[0,1]$ which are given by:

$$\mathcal{M}_{3,\alpha}(x,y,z) = \alpha \begin{bmatrix} h_1^{-2}(x,y,z) & 0 & 0 \\ 0 & h_2^{-2}(x,y,z) & 0 \\ 0 & 0 & h_3^{-2}(x,y,z) \end{bmatrix},$$

where $h_1(x,y,z) = 0.1(x+1)+0.05(x-1)$, $h_2(x,y,z) = 0.2$ and $h_3(x,y,z) = 0.2(z+2)$. The parameter α is used to control the level of accuracy of the mesh. The continuous

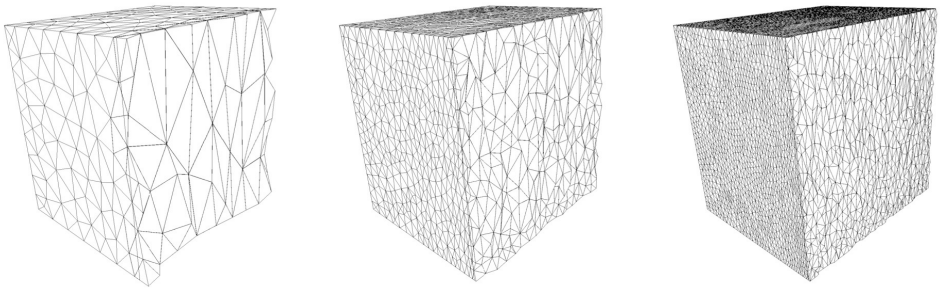

FIG. 1.5. *3D unit meshes* $\{\mathcal{H}_{3,\alpha}\}_\alpha$ *with respect to* $\{\mathbf{M}_3(\alpha)\}_\alpha$ *for* $\alpha = \{1, 8, 32\}$ *from left to right.*

mesh becomes coarser when α decreases. This trend is given by the computation of the complexity $\mathcal{C}(\mathbf{M}_3(\alpha))$:

$$\mathcal{C}(\mathbf{M}_3(\alpha)) = N(\alpha) = \iiint_{\Omega_3} \frac{1}{h_1 h_2 h_3}(x,y,z)\,\mathrm{d}x\mathrm{d}y\mathrm{d}z = \frac{1000}{3}\ln(2)(\ln(3)-\ln(2))\alpha^{\frac{3}{2}}.$$

We consider the interpolation error of the function u_4 given by:

$$u_4(x,y,z) = e^{2x+y+z}.$$

The point-wise continuous linear interpolation error is

$$(u_4 - \pi_{\mathcal{M}_{3,\alpha}} u_4)(x,y,z) = \frac{1}{10^5}\,\frac{e^{2\,x+y+z}\left(441\,x^2+798\,x+2361+400\,z^2+1600\,z\right)}{\alpha}.$$

Integration over Ω_3 leads to:

$$\begin{aligned}\iiint_{\Omega_3} |u_4 - \pi_{\mathcal{M}_{3,\alpha}} u_4|(x,y,z)\,\mathrm{d}x\mathrm{d}y\mathrm{d}z &= \frac{\left(-2133-1772\,e^4+7466\,e^2-10322\,e^6+6761\,e^8\right)}{4.\ 10^5\,e^4\,\alpha} \\ &\approx \frac{0.73}{\alpha} \approx \frac{126.215}{N(\alpha)^{\frac{2}{3}}}.\end{aligned}$$

Sequence of unit meshes with respect to $\mathbf{M}_3(\alpha)$ for $\alpha \in \{2, 4, 8, 16, 32\}$ have been generated using `Yams` [11] and `Gamanic` [12], see Figure 1.5. In this example, the constant linking the number of vertices and the continuous complexity is 2.07, see Figure 1.6 (left). Consequently, the perfect theoretical case is almost reached. The comparison between discrete and continuous interpolation error is depicted in Figure 1.6 (right). As for the 2D examples, we observe an excellent correlation between the continuous model and the numerical computation.

A numerical example. The theory is now applied to a more realistic 3D example where the continuous interpolation error results from numerical computations and not from an analytical evaluation which is not possible in that case. More precisely, the function and the continuous mesh (*i.e.,* the metric field) are linearly interpolated on a discrete mesh. Then, the continuous interpolation error is evaluated using these discrete data. This case is more representative of the practical use of the continuous mesh model. The aim of this example is to point out that, even with numerical computations, the continuous mesh model turns out to be a reliable model to predict interpolation error.

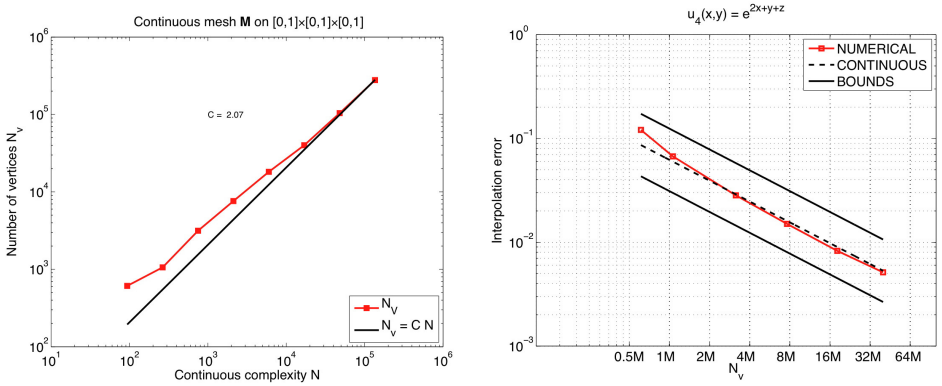

FIG. 1.6. *Left, comparison between the continuous mesh complexity and the number of vertices for a sequence of unit meshes* $\{\mathcal{H}_{3,\alpha}\}_\alpha$ *with respect to* $\{\mathbf{M}_3(\alpha)\}_\alpha$ *on* Ω_3*. Right, comparison between the continuous interpolation error* $\|u_4 - \pi_{\mathcal{M}_{3,\alpha}} u_4\|_{\mathbf{L}^1(\Omega_3)}$ *and the discrete interpolation error* $\|u_4 - \Pi_h u_4\|_{\mathbf{L}^1(\Omega_{3,h})}$.

We first define the continuous mesh $\mathbf{M}_4(\alpha) = (\mathcal{M}_{4,\alpha}(\mathbf{x}))$ on the domain $\Omega_4 = [-1,1]\times[-1,1]\times[-1,1] \subset \mathbb{R}^3$. The analytical expression of $\mathcal{M}_{4,\alpha}$ is inherited from the following quadratic form:

$$q(x,y,z) = 2x^2 - yx + 6y^2 + z^2.$$

The gradient vector is denoted $\mathbf{g}(x,y,z) = {}^t\left(\frac{\partial q}{\partial x}, \frac{\partial q}{\partial y}, \frac{\partial q}{\partial z}\right)$. The local Frenet frame is given by $F = (\mathbf{n}, \mathbf{t}_1, \mathbf{t}_2)$, where the vectors $\mathbf{t}_1, \mathbf{t}_2$ lies in the plane orthogonal to $\mathbf{n} = \mathbf{g}/\|\mathbf{g}\|_2$. We assume that $(\mathbf{t}_1, \mathbf{t}_2)$ is an orthonormal basis of $\mathbb{R}^2$. We also consider the Hessian matrix H_q of q:

$$H_q = \begin{bmatrix} 4 & -1 & 0 \\ -1 & 12 & 0 \\ 0 & 0 & 2 \end{bmatrix}.$$

From this matrix, we define the sub-matrix:

$$\overline{H}_q = \begin{bmatrix} {}^t\mathbf{t}_1 H_q \mathbf{t}_1 & {}^t\mathbf{t}_1 H_q \mathbf{t}_2 \\ {}^t\mathbf{t}_1 H_q \mathbf{t}_2 & {}^t\mathbf{t}_2 H_q \mathbf{t}_2 \end{bmatrix},$$

which is the projection of H_q onto the plane defined by $(\mathbf{t}_1, \mathbf{t}_2)$. We denote by $\overline{\lambda_1}$ and $\overline{\lambda_2}$ the eigenvalues of $\overline{H}_q$. The continuous mesh $\mathbf{M}_4(\alpha)$ parametrized by α is then given by:

$$\mathcal{M}_{4,\alpha} = F \begin{bmatrix} \alpha^2 \|\mathbf{g}\|_2^2 & & \\ & \alpha \dfrac{|\overline{\lambda_1}|}{2\|\mathbf{g}\|_2} & \\ & & \alpha \dfrac{|\overline{\lambda_2}|}{2\|\mathbf{g}\|_2} \end{bmatrix} {}^t F.$$

The complexity of $\mathbf{M}_4(\alpha)$ is:

$$\mathcal{C}(\mathbf{M}_4(\alpha)) = \frac{\alpha^2}{2} \int_\Omega \sqrt{\|\mathbf{g}\|_2^2 \, |\overline{\lambda_1}| \, |\overline{\lambda_2}|}\,,$$

which can be evaluated numerically. This continuous mesh has the physical feature to follow the iso-surfaces of the function q and to adapt the sizes to the local curvature of the iso-surfaces. The iso-surfaces of q are represented in Figure 1.7 (left). A sequence of unit meshes $\{\mathcal{H}_{4,\alpha}\}_\alpha$ with respect to $\{\mathbf{M}_4(\alpha)\}_\alpha$ for a complexity of

$$[4\,000,\ 8\,000,\ 16\,000,\ 32\,000,\ 64\,000,\ 128\,000]\,,$$

has been generated. Resulting unit meshes are depicted in Figure 1.8. In this case, the number of vertices is almost 2.3 times the continuous complexity.

We consider the interpolation error of the quadratic function:

$$u_5(x,y,z) = x^2 + y^2 + z^2\,.$$

In this case, the continuous interpolation error on the continuous mesh $\mathbf{M}_4(\alpha) = (\mathcal{M}_{4,\alpha}(\mathbf{x}))_{\mathbf{x}\in\Omega}$ cannot be anymore calculated analytically. We propose to compute it numerically on a given discrete mesh $\mathcal{H}$ as follow:

$$\int_\Omega |u_5(\mathbf{x}) - \pi_{\mathcal{M}_{4,\alpha}} u_5(\mathbf{x})|\,\mathrm{d}\mathbf{x} \approx \frac{1}{10}\sum_{K\in\mathcal{H}} |K|\,\mathrm{trace}\left(\mathcal{M}_{4,\alpha}(K)^{-\frac{1}{2}}\,|H_{u_5}(K)|\,\mathcal{M}_{4,\alpha}(K)^{-\frac{1}{2}}\right), \quad (1.1)$$

where $\mathcal{M}_{4,\alpha}(K)$ and $|H_{u_5}(K)|$ are the linear discrete representation on the element K of the continuous mesh and of the Hessian of u_5, thus a simple 1-order Gauss quadrature numerical integration is considered.

The discrete interpolation error of function u_5 is computed on the sequence of discrete meshes $\{\mathcal{H}_{4,\alpha}\}_\alpha$. These discrete errors are compared to continuous interpolation errors evaluated on a fine uniform mesh of constant size $h = 0.004$ using Relation (1.1). This size corresponds to the minimal size prescribed by the continuous mesh $\mathbf{M}_4(128\,000)$. The correlation between the continuous interpolation error and the discrete interpolation error is shown in Figure 1.7 (right). As expected, the order of convergence is well predicted but the numerical computations induces an over error estimation. Consequently, if the slope (*i.e.,* the convergence order) of the error is well approximated, the perfect fitting due the approximated evaluations of C_u results in a slightly shifted curve.

1.4. Some conclusions. These examples reveal that the interpolation error can be computed continuously without any discrete support. From this point of view, a discrete mesh is simply the projection of the continuous one. Discrepancies between continuous and discrete interpolation errors are due to projection errors. Practically, this gap depends on the mesh generator used and the difficulty to generate the desired unit mesh.

When the continuous interpolation error cannot be anymore evaluated analytically, we have shown that a numerical evaluation using a discrete mesh still provides accurate predictions of either the convergence order or the error magnitude.

Using this accurate and generic continuous interpolation error, we address in the next section the problem of minimizing the interpolation error in $\mathbf{L}^p$ norm on Ω.

2. Optimal control of the interpolation error in $\mathbf{L}^p$ norm. Using the definition of the linear continuous interpolate $\pi_{\mathcal{M}}$ given by Corollary 3.4 in [16], the following 3D point-wise interpolation error for u on $\mathbf{M} = (\mathcal{M}(\mathbf{x}))_{\mathbf{x}\in\Omega}$ is obtained:

$$e_{\mathcal{M}}(\mathbf{x}) = (u - \pi_{\mathcal{M}} u)(\mathbf{x}) \quad = \quad \frac{1}{10}\sum_{i=1}^{3} h_i^2(\mathbf{x})\,{}^t\mathbf{v}_i(\mathbf{x})\,|H_u(\mathbf{x})|\,\mathbf{v}_i(\mathbf{x}),$$

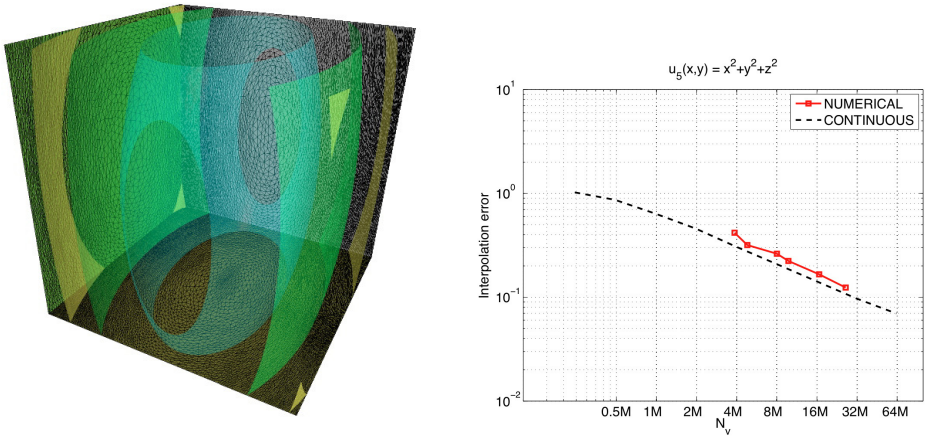

FIG. 1.7. *Left, iso-surfaces of function q. Right, comparison between the continuous interpolation error* $\|u_5 - \pi_{\mathcal{M}_{4,\alpha}} u_5\|_{\mathbf{L}^1(\Omega_4)}$ *and the discrete interpolation error* $\|u_5 - \Pi_h u_5\|_{\mathbf{L}^1(\Omega_{4,h})}$. *In this case, the continuous interpolation error is computed numerically by means of the linear approximation of the continuous mesh on a fine uniform discrete mesh.*

FIG. 1.8. *From left to right, views (cut through the plane* $y = 0$*) of the unit meshes* $\{\mathcal{H}_{4,\alpha}\}_\alpha$ *with respect to* $\{\mathbf{M}_4(\alpha)\}_\alpha$ *for a complexity of* 4000, 8000 *and* 16000.

where H_u is the Hessian of u, $(\mathbf{v}_i)_{i=1,3}$ the local eigen-directions of $\mathbf{M}$ and $(h_i)_{i=1,3}$ the local sizes of $\mathbf{M}$ along these directions. It is then possible to set the well-posed global optimization problem of finding the optimal continuous mesh minimizing the continuous interpolation error in $\mathbf{L}^p$ norm:

$$\text{Find } \mathbf{M}_{\mathbf{L}^p} = \min_{\mathbf{M}} E_p(\mathbf{M}) = \left(\int_\Omega e_{\mathcal{M}}^p \right)^{\frac{1}{p}} = \left(\int_\Omega (u - \pi_{\mathcal{M}} u)^p \right)^{\frac{1}{p}}, \tag{2.1}$$

under the constraint

$$\mathcal{C}(\mathbf{M}) = \int_\Omega d = N.$$

The constraint on the complexity is added to avoid the trivial solution where all $(h_i)_{i=1,3}$ are zero which provides a null error. Contrary to a discrete analysis, this problem can be solved globally by using a calculus of variations that is well-defined on the space of continuous meshes. In the following, to simplify the notations, we denote by $\gamma_i = {}^t\mathbf{v}_i(\mathbf{x}) \left| H_u(\mathbf{x}) \right| \mathbf{v}_i(\mathbf{x})$, for $i = 1, 3$. These positive scalar quantities measure the alignment between H_u and the directions of the continuous mesh given by $(\mathbf{v}_i)_{i=1,3}$.

Optimization problem (2.1) is solved in two steps. First, in Section 2.1, Problem (2.1) is solved for the subset of continuous meshes having the same fixed $(\gamma_i)_{i=1,3}$, in other words we seek for the $(h_i)_{i=1,3}$ solution of (2.1). Then, in Section 2.3, the optimal directions $(\mathbf{v}_i)_{i=1,3}$ are derived.

2.1. Formal resolution. In this section, Problem (2.1) is solved for the subset of continuous meshes having the same fixed $(\gamma_i)_{i=1,3}$. The resolution is based on an one-to-one change of variables using the decomposition of Proposition 2.4 defined in [16].

The density d and the first two anisotropic quotients $(r_i)_{i=1,2}$ are considered instead of the original unknowns $(h_i)_{i=1,3}$. The one-to-one mapping is then given by:

$$h_i = d^{-\frac{1}{3}} r_i^{\frac{1}{3}} \text{ for } i = 1,2 \text{ and } h_3 = (r_1\, r_2\, d)^{-\frac{1}{3}},$$

With this new set of unknowns, function $e_{\mathcal{M}}$ locally writes:

$$e_{\mathcal{M}} = \frac{1}{10}\, d^{-\frac{2}{3}} \left(r_1^{\frac{2}{3}} \gamma_1 + r_2^{\frac{2}{3}} \gamma_2 + (r_1\, r_2)^{-\frac{2}{3}} \gamma_3 \right), \tag{2.2}$$

thus, we have to solve:

$$\min_{((r_i)_i,\, d)} \int_\Omega d^{-\frac{2p}{3}} \left(r_1^{\frac{2}{3}} \gamma_1 + r_2^{\frac{2}{3}} \gamma_2 + (r_1\, r_2)^{-\frac{2}{3}} \gamma_3 \right)^p,$$

under the linear constraint:

$$\int_\Omega d \,= N. \tag{2.3}$$

One main consequence of considering d as an unknown is to have now a linear constraint, so that Problem (2.1) becomes convex. This one-to-one mapping also leads to an uncoupled problem: the optimal anisotropic quotients $(r_i)_{i=1,2}$ are first exhibited and the optimal density is derived in a second step.

The classical Euler-Lagrange necessary condition states that the variation of E_p at point $\mathbf{M}$ in direction $\delta\mathbf{M}$ is proportional to the variation of the constraint $\mathcal{C}$ in the neighborhood of a critical point. As we use a formal approach, the variation of E_p is approximated by:

$$\delta E_p(\mathbf{M}; \delta\mathbf{M}) = \lim_{\varepsilon \to 0} \frac{1}{\varepsilon} \left(\int_\Omega e^p_{\mathcal{M}+\varepsilon\delta\mathcal{M}} - \int_\Omega e^p_{\mathcal{M}} \right) \approx \int_\Omega \frac{\partial e^p_{\mathcal{M}}}{\partial \mathcal{M}}\, \delta\mathcal{M}.$$

As we have an equality constraint, the variation of $\mathcal{C}$ is null, so that the necessary Euler-Lagrange condition simplifies to $\delta E_p(\mathbf{M}; \delta\mathbf{M}) = 0$ and $\delta\mathcal{C}(\mathbf{M}; \delta\mathbf{M}) = 0$ for all $\delta\mathbf{M}$. For the variation $\delta\mathbf{M} = ((\delta r_i)_{i=1,2}, \delta d)$, it comes:

$$\forall \delta r_1,\ \forall \delta r_2,\ \forall \delta d \text{ with } \int \delta d = 0 \ \text{ we have } \ \sum_{i=1}^{2} \delta E_p(\mathbf{M}; \delta r_i) + \delta E_p(\mathbf{M}; \delta d) = 0. \tag{2.4}$$

If (Γ) stands for $\left(r_1^{\frac{2}{3}} \gamma_1 + r_2^{\frac{2}{3}} \gamma_2 + (r_1\, r_2)^{-\frac{2}{3}} \gamma_3 \right)$, (2.4) leads to :

$$\sum_{i=1}^{2} \delta E_p(\mathbf{M}; \delta r_i) = \int_\Omega \frac{2p}{3} d^{-\frac{2p}{3}} (\Gamma)^{p-1} \left(\sum_{i=1}^{2} \left(r_i^{-\frac{1}{3}} \gamma_i - (r_1\, r_2)^{-\frac{2}{3}} r_i^{-1} \gamma_3 \right) \delta r_i \right) = 0, \tag{2.5}$$

with the legal choice $\delta d = 0$. A particular condition to ensure (2.5) is given by :

$$\left\{ \begin{array}{l} r_1^{-\frac{1}{3}}\,\gamma_1 = (r_1\,r_2)^{-\frac{2}{3}}\,r_1^{-1}\gamma_3 \\ r_2^{-\frac{1}{3}}\,\gamma_2 = (r_1\,r_2)^{-\frac{2}{3}}\,r_2^{-1}\gamma_3 \end{array} \right. \Longrightarrow (r_1\,r_2)^{-1} = \frac{(\gamma_1\,\gamma_2)^{\frac{1}{2}}}{\gamma_3} \Longrightarrow \left\{ \begin{array}{l} r_1 = \gamma_1^{-1}\,\gamma_2^{\frac{1}{2}}\,\gamma_3^{\frac{1}{2}} \\ r_2 = \gamma_1^{\frac{1}{2}}\,\gamma_2^{-1}\,\gamma_3^{\frac{1}{2}}. \end{array} \right.$$

Previous equalities are used to simplify the initial expression of $e_{\mathcal{M}}$ given by (2.2):

$$e_{\mathcal{M}} = d^{-\frac{2}{3}} \left(r_1^{\frac{2}{3}}\gamma_1 + r_2^{\frac{2}{3}}\gamma_2 + (r_1\,r_2)^{-\frac{2}{3}}\gamma_3 \right) = 3\,d^{-\frac{2}{3}}\,(\gamma_1\,\gamma_2\,\gamma_3)^{\frac{1}{3}}\,.$$

Relation (2.4) for the legal choices $\delta r_i = 0$ for $i = 1, 2$ leads to:

$$\delta E_p(\mathbf{M}; \delta d) = \int_\Omega \frac{2p}{3}\,3^p\,d^{-\frac{2p+3}{3}}\,(\gamma_1\,\gamma_2\,\gamma_3)^{\frac{p}{3}}\,\delta d \;= 0 \;\text{ with }\; \int_\Omega \delta d = 0. \tag{2.6}$$

A condition to ensure (2.6) is given by $d^{-\frac{2p+3}{3}}\,(\gamma_1\,\gamma_2\,\gamma_3)^{\frac{p}{3}} = Cte$ where Cte is a real constant. Using the constraint on the complexity defined by (2.3), the final expression of d is:

$$d = N \left(\int_\Omega (\gamma_1\,\gamma_2\,\gamma_3)^{\frac{p}{2p+3}} \right)^{-1} (\gamma_1\,\gamma_2\,\gamma_3)^{\frac{p}{2p+3}}\,.$$

Finally, the optimal continuous mesh $\mathbf{M}^*$ solution of (2.1) is given by:

$$\begin{array}{l} \lambda_i^* = (h_i^*)^{-2} = N^{\frac{2}{3}} \left(\displaystyle\int_\Omega (\gamma_1\,\gamma_2\,\gamma_3)^{\frac{p}{2p+3}} \right)^{-\frac{2}{3}} (\gamma_1\,\gamma_2\,\gamma_3)^{-\frac{1}{2p+3}}\;\gamma_i\,, \\ \text{and} \quad r_i^* = \dfrac{(\gamma_1\,\gamma_2\,\gamma_3)^{\frac{1}{2}}}{\gamma_i^{\frac{3}{2}}} \;\; \forall i = 1 \ldots 3\,. \end{array} \tag{2.7}$$

2.2. Uniqueness. We now prove that the optimal continuous mesh defined by (2.7) is the unique solution of Problem (2.1) verifying $E_p(\mathbf{M}^*)^p \leq E_p(\mathbf{M})^p$ for all $\mathbf{M}$ having the same fixed $(\gamma_i)_{i=1,3}$. We can evaluate E_p to the power p at the optimal point $\mathbf{M}^*$, it comes:

$$E_p(\mathbf{M}^*)^p = 3^p N^{-\frac{2p}{3}} \left(\int_\Omega (\gamma_1\,\gamma_2\,\gamma_3)^{\frac{p}{2p+3}} \right)^{\frac{2p+3}{3}}. \tag{2.8}$$

A generic $\mathbf{M}$ of complexity N is given by its three anisotropic quotients $(r_i)_{i=1,3}$ and its density d. To take into account the constraint on the density, the density is rewritten as: $d = N(\int_\Omega f)^{-1} f$, where f is a strictly positive function. The error committed with $\mathbf{M}$ is then:

$$E_p(\mathbf{M})^p = N^{-\frac{2p}{3}} \left(\int_\Omega f \right)^{-\frac{2p}{3}} \int_\Omega f^{-\frac{2p}{3}} \left(r_1^{\frac{2}{3}}\gamma_1 + r_2^{\frac{2}{3}}\gamma_2 + r_3^{\frac{2}{3}}\gamma_3 \right)^p.$$

To prove $E_p(\mathbf{M}^*)^p \leq E_p(\mathbf{M})^p$, we use the generalized arithmetic-geometric inequality which comes from the concavity of ln:

$$\ln\left(\frac{1}{3}\sum_{i=1}^3 r_i^{\frac{2}{3}}\gamma_i \right) \geq \frac{1}{3}\sum_{i=1}^3 \ln\left(r_i^{\frac{2}{3}}\gamma_i \right) = \ln\left(\prod_{i=1}^3 \gamma_i^{\frac{1}{3}} \right) \;\Longrightarrow\; \left(\sum_{i=1}^3 r_i^{\frac{2}{3}}\gamma_i \right)^p \geq 3^p \left(\prod_{i=1}^3 \gamma_i^{\frac{1}{3}} \right)^p,$$

as $r_1\, r_2\, r_3 = 1$. Finally, if we denote $g = (\gamma_1\, \gamma_2\, \gamma_3\,)^{\frac{p}{2p+3}}$, we have:

$$\left\{ \begin{array}{lcl} E(\mathbf{M}^*)^{\frac{3p}{2p+3}} & = & 3^{\frac{3p}{2p+3}} N^{-\frac{2p}{2p+3}} \displaystyle\int_\Omega g\,, \\ \\ E(\mathbf{M})^{\frac{3p}{2p+3}} & \geq & 3^{\frac{3p}{2p+3}} N^{-\frac{2p}{2p+3}} \left(\displaystyle\int_\Omega f\right)^{\frac{2p}{2p+3}} \left(\displaystyle\int_\Omega f^{-\frac{2p}{3}} g^{\frac{2p+3}{3}}\right)^{\frac{3}{2p+3}}. \end{array} \right.$$

Using the Hölder inequality, it comes:

$$\begin{aligned} \left(\int_\Omega f\right)^{\frac{2p}{2p+3}} \left(\int_\Omega f^{-\frac{2p}{3}} g^{\frac{2p+3}{3}}\right)^{\frac{3}{2p+3}} &= \left(\int_\Omega f\right)^{\frac{2p}{2p+3}} \left(\int_\Omega \left(\frac{g}{f^{\frac{2p}{2p+3}}}\right)^{\frac{2p+3}{3}}\right)^{\frac{3}{2p+3}} \\ &\geq \left(\int_\Omega f^{\frac{2p}{2p+3}} \left(\frac{g}{f^{\frac{2p}{2p+3}}}\right)\right) = \int_\Omega g\,, \end{aligned} \tag{2.9}$$

as $\dfrac{2p+3}{2p} \geq 1$, $\dfrac{2p+3}{3} \geq 1$ and $\dfrac{2p}{2p+3} + \dfrac{3}{2p+3} = 1$. Relation (2.9) implies $E_p(\mathbf{M}^*) \leq E_p(\mathbf{M})$ for all $\mathbf{M}$ having the same fixed $(\gamma_i)_{i=1,3}$. As Problem (2.1) is strictly convex, the optimal solution $\mathbf{M}^*$ is unique.

2.3. Optimal orientations. For a given set of directions $(\mathbf{v}_i)_{i=1,3}$, the optimal interpolation error reads:

$$\|u - \pi_{\mathcal{M}^*} u\|_{\mathbf{L}^p(\Omega)} = 3N^{-\frac{2}{3}} \left(\int_\Omega (\det(\Gamma))^{\frac{p}{2p+3}}\right)^{\frac{2p+3}{3p}},$$

where Γ is the diagonal matrix composed of $(\gamma_i)_{i=1,3}$. It is then possible to minimize the previous error by seeking the directions $\mathbf{v}_i$ minimizing $\det(\Gamma)^{\frac{p}{2p+3}}$, or equivalently minimizing $\det(\Gamma)$. Geometrically, $\det(\Gamma)$ is simply the volume of the parallelepiped defined by $(\mathbf{v}_i)_{i=1,3}$ and of length $({}^t\mathbf{v}_i\, |H_u| \mathbf{v}_i)_{i=1,3}$. We denote by $(\lambda_i)_{i=1,3}$ the eigenvalues of $|H_u|$ and $(\mathbf{u}_i)_{i=1,3}$ its principal directions. The length of a side computed with respect to $|H_u|$ is:

$${}^t\mathbf{v}_1\, |H_u|\, \mathbf{v}_1 \;=\; \sum_{k=1}^{3} \lambda_k \left({}^t\mathbf{v}_1\, \mathbf{u}_k\right)^2 \;\geq\; \min_{k=1,3} (|\lambda_k|).$$

The previous length is minimal when $\mathbf{v}_1$ is aligned with the eigenvector corresponding to the smallest eigenvalues. We can repeat this procedure among the remaining directions by always aligning the remaining $\mathbf{v}_i$ with the direction associated with the remaining smallest eigenvalue. It results that $\det(\Gamma)^{\frac{p}{2p+3}}$, is minimal when the vectors $(\mathbf{v}_i)_{i=1,3}$ are aligned with the principal directions of $|H_u|$. We conclude that the optimal metric both in sizes and directions is given by:

THEOREM 2.1. *Let u be a twice continuously differentiable function defined on $\Omega \subset \mathbb{R}^3$, H_u its Hessian, the optimal continuous mesh $\mathbf{M}_{\mathbf{L}^p}(u)$ minimizing Problem (2.1) reads locally:*

$$\mathcal{M}_{\mathbf{L}^p} = D_{\mathbf{L}^p}\ \det(|H_u|)^{\frac{-1}{2p+3}}\, |H_u|, \ \textit{with}\ D_{\mathbf{L}^p} = N^{\frac{2}{3}} \left(\int_\Omega \det(|H_u|)^{\frac{p}{2p+3}}\right)^{-\frac{2}{3}}. \tag{2.10}$$

It verifies the following properties:

- $\mathbf{M}_{\mathbf{L}^p}(u)$ *is unique*
- $\mathbf{M}_{\mathbf{L}^p}(u)$ *is locally aligned with the eigenvectors basis of* H_u *and has the same anisotropic quotients as* H_u
- $\mathbf{M}_{\mathbf{L}^p}(u)$ *provides an optimal explicit bound of the interpolation error in* $\mathbf{L}^p$ *norm:*

$$\|u - \pi_{\mathcal{M}_{\mathbf{L}^p}} u\|_{\mathbf{L}^p(\Omega)} = 3\, N^{-\frac{2}{3}} \left(\int_\Omega \det\left(|H_u|\right)^{\frac{p}{2p+3}} \right)^{\frac{2p+3}{3p}}. \tag{2.11}$$

- *For a sequence of continuous meshes having an increasing complexity with the same orientation and anisotropic quotients* $(\mathbf{M}^N_{\mathbf{L}^p}(u))_{N=1\ldots\infty}$*, the asymptotic order of convergence verifies:*

$$\|u - \pi_{\mathcal{M}^N_{\mathbf{L}^p}} u\|_{\mathbf{L}^p(\Omega)} \leq \frac{Cst}{N^{2/3}}. \tag{2.12}$$

Relation (2.12) points out a global second order of mesh convergence.

Note that Bound (2.11) has been also derived in [7]. However, in our case, all the constants of (2.11) are explicitly given. In addition, a second order of convergence is predicted. Note the family of optimal continuous meshes parametrized by N defines a class of embedded continuous meshes in the sense of Definition 2.5 defined in [16]. The last difference with [7] is that we are able to practically generate a discrete mesh approximating the continuous optimal solution by using any metric-based adaptive mesh generators as soon as the generated mesh satisfies Definition 2.7.

Note that passing to the limit for $p \to \infty$ leads to the classical metric that controls the interpolation error in $\mathbf{L}^\infty$ as used in [6, 10].

We now provide bounds on the discrete interpolation error when the continuous mesh is projected into the space of discrete meshes by means of an adaptive mesh generator. If the mesh generator achieves a unit mesh with respect to $\mathbf{M}_{\mathbf{L}^p}$ in the sense of Definition 2.6 and 2.7 of [16], then we have the following bounds for the discrete interpolation error:

$$\frac{1}{2}\|u - \pi_{\mathcal{M}_{\mathbf{L}^p}} u\|_{\mathbf{L}^p(\Omega)} \leq \|u - \Pi_h u\|_{\mathbf{L}^p(\Omega_h)} \leq 2\,\|u - \pi_{\mathcal{M}_{\mathbf{L}^p}} u\|_{\mathbf{L}^p(\Omega)},$$

or equivalently,

$$\frac{3}{2}\, N^{-\frac{2}{3}} \left(\int_\Omega \det\left(|H_u|\right)^{\frac{p}{2p+3}} \right)^{\frac{2p+3}{3p}} \leq \|u - \Pi_h u\|_{\mathbf{L}^p(\Omega_h)} \leq 6\, N^{-\frac{2}{3}} \left(\int_\Omega \det\left(|H_u|\right)^{\frac{p}{2p+3}} \right)^{\frac{2p+3}{3p}}.$$

In other words, $\mathbf{M}_{\mathbf{L}^p}$ defined by Relation (2.10) allows us to generate an optimal adapted mesh to control the interpolation error in $\mathbf{L}^p$ norm.

When dealing with solutions of a PDE, the current error estimate is not anymore certified as in classical adaptive finite element based on *a posteriori* estimates [3]. However, the prescription of the anisotropy is natural and does not need to be transformed into a metric tensors field as done for *a posteriori* estimates [18] to be able to practically generate quality anisotropic meshes. However, one advantage is that this approach is completely generic and does not depend on the PDE at hand.

3. Application to multiscale mesh adaptation. The previous section has provided an analytical expression, cf. Theorem 2.1, of the optimal continuous mesh controlling the linear interpolation error in $\mathbf{L}^p$-norm for a fixed complexity. Now, we use this main result in the context of anisotropic mesh adaptation. In section 3.3, mesh adaptation is considered for analytical functions and, Section 3.4, we deal with numerical solutions provided by the resolution of PDEs.

For the analytic function case, the mesh adaptation process is carried out *via* a mesh adaptation loop inside which an algorithmic convergence of the pair mesh-solution is sought. At each iteration of the adaptation loop, the analytical function u is applied or projected on the current discrete mesh meaning that $u_h = \Pi_h u$. The optimal continuous mesh $\mathbf{M}_{\mathbf{L}^p}$ is then derived from this discrete representation of the analytical function. We obtain a discrete definition of $\mathbf{M}_{\mathbf{L}^p}$ on the current mesh. Next, a new adapted discrete mesh is generated according to continuous mesh $\mathbf{M}_{\mathbf{L}^p}$. That is to say, a unit mesh is generated with respect to Riemannian metric field $\mathbf{M}_{\mathbf{L}^p}$. This procedure is repeated until the convergence of the pair mesh-solution is reached.

In the context of numerical solutions provided by the resolution of PDEs, the difference lies in the evaluation of u_h. Once a new adapted mesh has been generated, the previous numerical solution is interpolated on this new mesh [2]. Then, the PDEs are solved again from this new initial state providing a new numerical solution u_h.

However, in both contexts, continuous mesh $\mathbf{M}_{\mathbf{L}^p}$ is derived from u_h which is represented by a piecewise linear function. Consequently, our analysis cannot be directly applied. Next section presents the numerical construction of $\mathbf{M}_{\mathbf{L}^p}$ in that case.

3.1. Application to solution given by numerical approximation. Let $\bar{V}_h^k$ be the space of piecewise polynomials of degree k and V_h^k be the space of continuous piecewise polynomials of degree k associated with a given mesh $\mathcal{H}$ of domain Ω_h. We denote by R_h a reconstruction operator applied to the numerical approximation u_h. We assume that the reconstruction $R_h u_h$ is better than u_h for a given norm $\|.\|$ in the sense that:

$$\|u - R_h u_h\| \leq \alpha \|u - u_h\| \quad \text{where} \;\; 0 \leq \alpha < 1 \,.$$

From the triangle inequality we deduce:

$$\|u - u_h\| \;\leq\; \frac{1}{1-\alpha} \|R_h u_h - u_h\| \,.$$

If the reconstruction operator R_h has the property:

$$\Pi_h R_h \phi_h = \phi_h \,, \quad \forall \phi_h \in V_h^1 \,, \tag{3.1}$$

we can then bound the approximation error of the solution by the interpolation error of the reconstructed function $R_h u_h$:

$$\|u - u_h\| \leq \frac{1}{1-\alpha} \|R_h u_h - \Pi_h R_h u_h\| \,. \tag{3.2}$$

From Theorem 2.1, we can exhibit the following upper bound of the approximation error:

$$\|u - u_h\| \leq \frac{6\, N^{-\frac{2}{3}}}{1-\alpha} \left(\int_\Omega \det \left(|H_{R_h u_h}| \right)^{\frac{p}{2p+3}} \right)^{\frac{2p+3}{3p}} \,.$$

In the general case, it is important to note that $\mathcal{M}_{\mathbf{L}^p}$ defined by (2.10) and applied to $R_h u_h$ does not allow us to generate an optimal adapted mesh to control the approximation error $\|u - u_h\|$. The approximation error is only controlled when all previous assumptions are verified. However, we aim at applying the analysis to the compressible Euler or Navier-Stokes systems for which there is nowadays no available anisotropic error estimate. Consequently, we consider our analysis that applies directly. The lack of a full theoretical support is then overcome by comparing numerical adaptive solutions with experiments, see Section 3.4 and [1, 17].

3.2. Reconstruction operator. In the context of numerical simulations, u_h lies in V_h^1 and its derivatives ∇u_h in $\bar{V}_h^0$. We propose a reconstruction operator from V_h^1 into V_h^2 based on P2-Lagrange finite element test functions. As approximate solution u_h is only known at mesh vertices, we need to reconstruct mid-edge values. To this end, we consider the $\mathbf{L}^2$-projection operator $\mathcal{P} \,:\, \bar{V}_h^0 \to V_h^1$ defined by [8]:

$$\nabla_R u_h = \mathcal{P}(\nabla u_h) = \sum_{\mathbf{p}_i} \nabla_R\, u_h(\mathbf{p}_i)\phi_i \quad \text{where} \quad \nabla_R\, u_h(\mathbf{p}_i) = \frac{\sum_{K_j \in S_i} |K_j| \nabla(u_{h|K_j})}{\sum_{K_j \in S_i} |K_j|}\,,$$

where $\mathbf{p}_i$ denotes the i^{th} vertex of mesh $\mathcal{H}$, S_i is the stencil of $\mathbf{p}_i$, ϕ the basis function of V_h^1 and $|K_j|$ denotes the volume of element K_j. These nodal recovered gradients are used to evaluate mid-edge values. For edge $\mathbf{e} = \mathbf{pq}$ the mid-edge value $u_h(\mathbf{e})$ is given by:

$$u_h(\mathbf{e}) = \frac{u_h(\mathbf{p}) + u_h(\mathbf{q})}{2} + \frac{\nabla_R u_h(\mathbf{p}) - \nabla_R u_h(\mathbf{q})}{8} \cdot \mathbf{pq}$$

which corresponds to a cubic reconstruction on each edge. The reconstructed function $R_h u_h$ of V_h^2 writes:

$$R_h u_h = \sum_{\mathbf{p}_i} u_h(\mathbf{p}_i)\psi_{\mathbf{p}_i} + \sum_{\mathbf{e}_j} u_h(\mathbf{e}_j)\psi_{\mathbf{e}_j}$$

where $\psi_{\mathbf{p}} = \phi_{\mathbf{p}}\,(2\,\phi_{\mathbf{p}} - 1)$ and $\psi_{\mathbf{e}} = 4\,\phi_{\mathbf{p}}\,\phi_{\mathbf{q}}$ are the P2-Lagrange test functions. This reconstructed function verifies by definition:

$$\Pi_h R_h u_h = u_h\,,$$

which is a required property, see (3.1).

Note that the Hessian of $R_h u_h$ lies in $\bar{V}_h^0$. If nodal values are needed to build $\mathcal{M}_{\mathbf{L}^p}$, then the $\mathbf{L}^2$-projection operator can be applied to these Hessian [8]. This recovery procedure is similar to the ones of [19, 20].

3.3. Case of analytical functions.
A smooth two-dimensional function. The first function f_1 is a smooth function involving variations of small and large amplitudes. The function is defined as follow:

$$f_1(x,y) = \begin{cases} 0.01\sin(50\,xy) & \text{if} & xy \le \dfrac{\pi}{50}, \\ \sin(50\,xy) & \text{else if} & xy \le 2\dfrac{\pi}{50}, \\ 0.01\sin(50\,xy) & \text{elsewhere.} & \end{cases}$$

This function is composed of variations having a unit amplitude along with small variations having an amplitude of 0.001. This feature is illustrated in Figure 3.1 (top left) where a cut through the line $y = 0$ is depicted.

The mesh adaptation process based on a control of the interpolation error is analyzed for the $\mathbf{L}^1$, $\mathbf{L}^2$ and $\mathbf{L}^4$ norms. Figure 3.1 shows adapted meshes composed of almost 7 000 vertices for each norm. We observe that the small amplitude waves regions are better captured when using a $\mathbf{L}^p$ norm with a lower p ($\mathbf{L}^1$ is the best) whereas the $\mathbf{L}^4$ norm ignores small amplitudes regions and clearly more refined large amplitudes areas. This behavior is due to the term $\det(|H_u|)^{\frac{-1}{2p+3}}$ in Relation (2.10) which gives more sensitivity to lower p norm. It illustrates that controlling the interpolation error in $\mathbf{L}^p$ norm with small p is crucial to capture all scales of the solution.

For each norm, mesh adaptations have been performed for a wide range of complexities leading to adapted meshes of sizes varying between 150 and 60 000 vertices in order to perform a convergence study. The resulting interpolation errors are plotted as a function of the number of vertices N_h in Figure 3.2 (left). Whatever the considered norm, several regions can be distinguished:

- for $N_h < 1000$, a second order convergence is obtained,
- for N_h from 1000 to 9000, the convergence order is lower or equal to one,
- for $N_h > 9000$, second order convergence is observed again.

This behavior is explained by the characteristics of function f_1. For low complexity, a second order of convergence is obtained because only the large scales of the solution contribute to the interpolation error. The error due to the solution small scales is negligible as compared to the unit amplitude waves. Therefore, the adaptive process only refines the large scales and ignores the small ones. However, once the complexity is large enough, the error for adapted meshes due to the small scales becomes of the same order as the error due to the large scales. A first order convergence is observed. These small scales are then captured by the adaptive process and the asymptotic second order of convergence is recovered.

The complexity or the number of vertices needed to reach the asymptotic theoretical order of convergence depends on the chosen norm. Indeed, as low p norm are more sensitive to small scales of the solution, small variations are earlier captured and the asymptotic order of convergence is earlier attained with lower p. For function f_1, the adaptive process in $\mathbf{L}^1$ norm reaches the asymptotic second order after 3 000 vertices whereas 9 000 vertices are necessary for $\mathbf{L}^4$ norm.

Asymptotic order of convergence. The aim of this second example is to illustrate why the $\mathbf{L}^\infty$ norm is not well-suited for solutions involving different scales. The considered function is:

$$\forall (x,y) \in [0,1]^2, \quad f_2(x,y) = 0.1\sin(50x) + \operatorname{atan}\left(\frac{0.1}{\sin(5y) - 2x}\right).$$

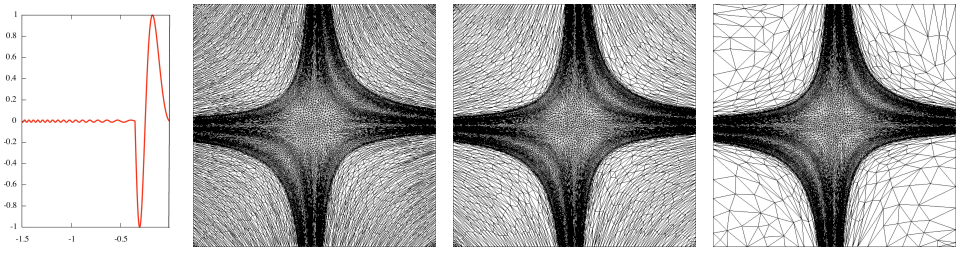

FIG. 3.1. *From left to right, representation of function f_1 along the cut line $y = 0$, optimal adapted meshes for norms $\mathbf{L}^1$, $\mathbf{L}^2$ and $\mathbf{L}^4$. Each mesh is composed of about 7 000 vertices.*

The function is composed of small amplitudes waves, given by the sine, going through a sinusoidal steep-gradient step (similar to a Dirac layer), induced by the atan, in the middle of the domain, see Figure 3.3 (left). This function is proposed to point out the attractive effect of a steep-gradient region on the mesh adaptation process. Two optimal adapted meshes have been generated: one controlling the $\mathbf{L}^1$ norm and the other controlling the $\mathbf{L}^\infty$ norm of the interpolation error. As illustrated in Figure 3.3, the mesh obtained with $\mathbf{L}^\infty$ norm only refines the steep-gradient region, whereas the $\mathbf{L}^1$ norm was able to capture the small amplitude waves. And this, for meshes composed of 100 000 vertices. This example points out again that mesh adaptation in $\mathbf{L}^p$ norm with a low p value is more appropriate to capture weak phenomena in simulations involving large amplitude phenomena such as shocks in CFD.

Moreover, Estimation (2.11) of the order of convergence is continuous. This means that the order of convergence holds asymptotically when the size of the mesh tends to zero. However, from a practical point of view, we hope that small complexities are sufficient to reach it. The previous example illustrates this point where 9 000 vertices were sufficient to reach the optimal order for all norms. On the contrary, this example reveals a practical situation where the asymptotic order of convergence cannot be reached for some norms and for a tractable number of vertices. Indeed, the order of convergence for f_2 in $\mathbf{L}^1$ and $\mathbf{L}^2$ norms is plotted in Figure 3.2 (right). If the $\mathbf{L}^1$ norm converges asymptotically with a second order rate, only a rate of one and a half is reached for the $\mathbf{L}^2$ norm.

A three-dimensional function. Function f_{3d} is a smooth function involving variations of small and large amplitudes. The function is defined as follows in a spherical domain:

$$f_{3d}(x,y,z) = \begin{cases} 0.1\,\sin(50\,\mathbf{x}) & \text{if } \mathbf{x} \leq \dfrac{-\pi}{50} \\ \sin(50\,\mathbf{x}) & \text{if } \dfrac{-\pi}{50} < \mathbf{x} \leq \dfrac{2\,\pi}{50} \\ 0.1\,\sin(50\,\mathbf{x}) & \text{if } \dfrac{2\,\pi}{50} < \mathbf{x} \end{cases} \tag{3.3}$$

where $\mathbf{x} = (x-0.4)\,(y-0.4)\,(z-0.4)$. As observed previously in two dimensions, the metric defined in $\mathbf{L}^1$ norm is more sensitive to the small amplitudes of the solution than norms with larger p. This is shown in Figure 3.4 where optimal anisotropic adapted meshes for a complexity equal to 275 000 are depicted for the $\mathbf{L}^1$, $\mathbf{L}^2$ and $\mathbf{L}^\infty$

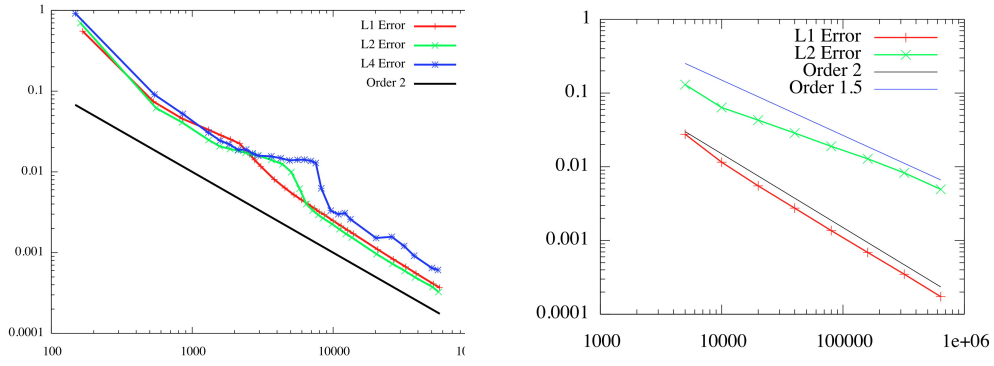

FIG. 3.2. *Plot of the linear interpolation error (ordinate) with respect to the number of vertices (abscissa) for functions f_1 (left) and f_2 (right). The order of convergence is also represented.*

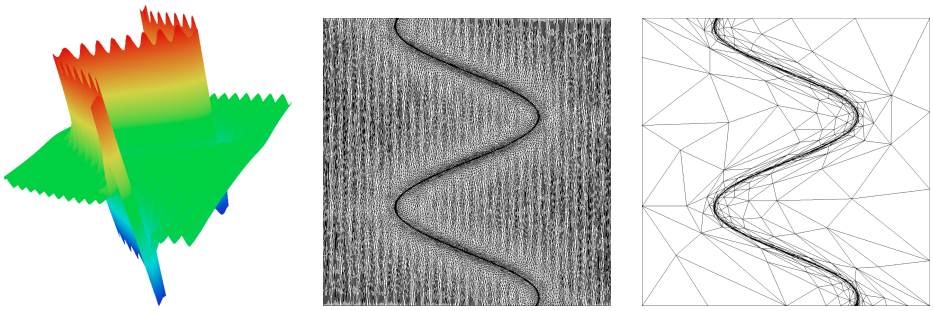

FIG. 3.3. *Left, representation of function* f_2. *Optimal adapted meshes, composed of almost* 100 000 *vertices, controlling the interpolation error in* $\mathbf{L}^1$ *norm (middle) and in* $\mathbf{L}^\infty$ *norm (right).*

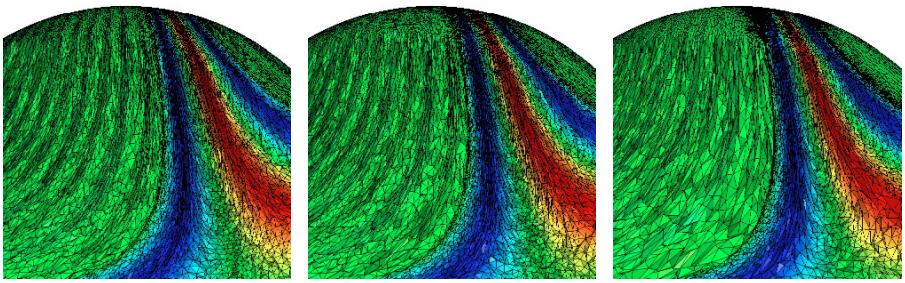

FIG. 3.4. *Optimal anisotropic adapted meshes for the* $\mathbf{L}^1$ *(left),* $\mathbf{L}^2$ *(middle) and* $\mathbf{L}^\infty$ *(right) norms for a complexity equal to* 275 000. *Views of the volume mesh in a cut plane.*

norms. The small variations of the function are clearly better captured with $\mathbf{L}^1$ norm than with $\mathbf{L}^\infty$ norm.

3.4. Case of numerical solutions of PDEs. When dealing with solutions of PDEs, the linear interpolation error is appropriate to control the error for second order accurate numerical schemes. Indeed, such numerical schemes are exact for linear solutions, thus the first (main) term of the error is the second order term involving the second order derivatives. In this section, the proposed adaptive procedure defined by Theoreom 2.1 is applied to predict and to capture accurately the numerical solution of a non-linear PDEs system given by the compressible Euler equations. The mesh adaptation is validated by comparing on an analytical geometry the numerical results to wind tunnel experiments.

The 3D compressible Euler system. In this example, we consider a supersonic flow around a body modeled by the compressible Euler equations. Assuming that the gas is perfect, inviscid and that there is no thermal diffusion, the Euler equations for mass, momentum and energy conservation read:

$$\left\{\begin{array}{rcl} \dfrac{\partial \rho}{\partial t} + \nabla.(\rho \mathbf{U}) & = & 0\,, \\ \dfrac{\partial (\rho \mathbf{U})}{\partial t} + \nabla.(\rho \mathbf{U} \otimes \mathbf{U}) + \nabla p & = & 0\,, \\ \dfrac{\partial (\rho E)}{\partial t} + \nabla.((\rho E + p)\mathbf{U}) & = & 0\,, \end{array}\right.$$

where ρ denotes the density, $\mathbf{U}$ the velocity vector, $E = T + \frac{\|\mathbf{U}\|^2}{2}$ the total energy

and $p = (\gamma-1)\rho T$ the pressure with $\gamma = 1.4$ the ratio of specific heats and T the temperature. The non-linear Euler system is solved with a second-order accurate in space and time Finite Volume numerical scheme on unstructured tetrahedral meshes [1].

Problem definition. Geometric model 8 of [13] is selected to validate the proposed adaptive approach. This model represents two tandem cones connected by a cylinder, it is defined analytically in inches by:

$$\begin{aligned} r &= x\sqrt{\frac{0.08}{\pi}} \quad \text{if} \quad 0 \le x \le 0.25\,l \\ r &= \sqrt{\frac{0.02}{\pi}} \quad \text{if} \quad 0.25\,l \le x \le 0.75\,l \\ r &= \frac{2}{2+\sqrt{2}}\sqrt{\frac{0.04}{\pi}}\left(x - \frac{2-\sqrt{2}}{2}\right) \quad \text{if} \quad 0.75\,l \le x \le l\,, \end{aligned}$$

with a reference length $l = 2$ inches (5.08 centimeters). The initial geometry has been elongated by adding a cylinder of length $2\,l$ to represent the sting support of the wind-tunnel. The geometry is immersed in a cylindrical domain aligned with the x-axis. The cylinder has a length of 6 meters (236 inches) and a radius of 2.5 meters (98 inches). The flow conditions are Mach 1.41 at 0° angle of attack. The numerical solution, *i.e.,* pressure signatures extracted along several lines at different distances under the geometry, is compared to experimental data obtained in wind-tunnel by NASA [13].

Optimal mesh adaptation and comparisons with experiments. The initial uniform mesh is composed of 243 446 vertices and 1 163 402 tetrahedra. As regards mesh adaptation, the Mach number is chosen as sensitive variable and its interpolation error is controlled in $\mathbf{L}^2$ norm. A total of 15 adaptation iterations are performed. They are split into 3 steps of 5 adaptations with an increasing complexity:

$$[200\,000,\ 400\,000,\ 800\,000].$$

At each step, the couple mesh-solution is algorithmically converged at a fixed complexity. Considering an increasing dynamic complexity level has the advantage to accelerate the convergence of the whole process. We compared the final solution obtained on the final adapted mesh of almost 5 millions vertices and 30 millions tetrahedra. To illustrate the anisotropic features of the meshes, the final mesh obtained at the end of the adaptive process is shown in Figure 3.5.

Results are analyzed by extracting the pressure signatures along lines at various distances under the geometry from 5 to 20 body lengths. More precisely, we plot:

$$\Delta p = \left(\frac{R}{l}\right)^{\frac{3}{4}} \frac{p - p_\infty}{p_\infty} \quad \text{as a function of} \quad \Delta x = \frac{x}{l}\left(\frac{R}{l}\right)^{-\frac{1}{4}},$$

where R the distance to the body. Signatures are compared against NASA experimental wind-tunnel data given in [13]. The agreement with experimental data is excellent, see Figure 3.6. Notice that in [13], it is specified that the rounding of the measured pressure peaks is believed to be due in part to wind-tunnel vibration and boundary layer effects. Therefore, sharper shock peaks obtained in our simulations are the good answer.

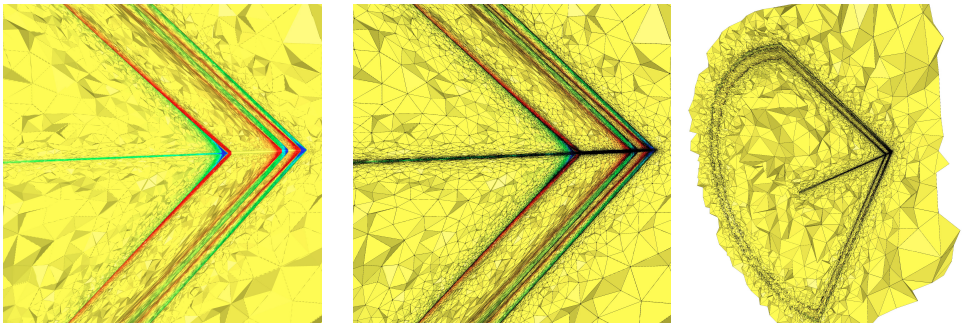

FIG. 3.5. *Views of the final adpated mesh and solution (local Mach number) for the two tandems cone geometry.*

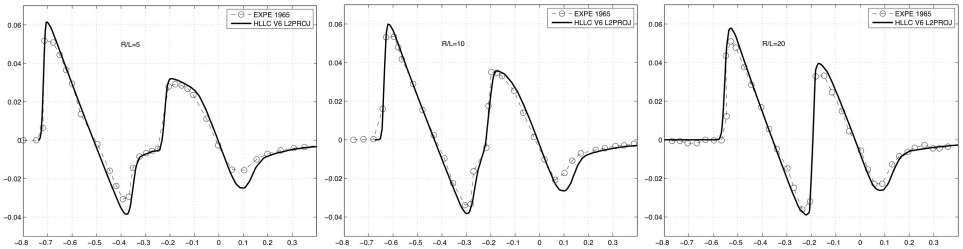

FIG. 3.6. *Comparison of pressure field computed on the adapted final solution with the experiments at various distances under the body.*

4. Conclusion. In this paper, we have given numerical validations of the continuous mesh framework introduced in [16]. The numerical examples have illustrated that, for a given continuous mesh (known analytically), we are able to compute the interpolation error of a given function on this continuous mesh without any discrete support. Consequently, the continuous mesh model demonstrates the well-foundedness of the metric-based mesh adaptation. The numerical examples have also shown that the continuous framework is able to predict perfectly the convergence order of the interpolation error on a sequence of continuous meshes.

This continuous model has then been used as the variable of the following global optimization problem:

$$\min_{\mathbf{M}} \left(\int_{\Omega} |u - \pi_{\mathcal{M}} u|^p \right)^{\frac{1}{p}},$$

subject to $\mathcal{C}(\mathbf{M}) = N$. The solution of this problem yields in the derivation of an optimal error bound for the interpolation error along with the prediction of a second order of convergence. In the mean time, a closed form of the optimal continuous mesh is also given. The latter is used to conduct anisotropic refinement. Numerical simulations and comparisons with experiments show the accuracy and the efficiency of this model to deal with anisotropic mesh adaptation.

This continuous mesh framework has been also successfully extended to the control of the approximation error on a functional output for goal-oriented anisotropic mesh adaptation. In this case, the PDE is explicitly taken into account in the analysis. This has been done for the set of Euler equations [17]. Currently, the authors are

addressing the extension of the present concept to functions in $\mathbf{H}^1$ and discontinuous functions.

REFERENCES

[1] F. Alauzet and A. Loseille, *High order sonic boom modeling by adaptive methods*, J. Comp. Phys., 229 (2010), pp. 561–593.

[2] F. Alauzet and M. Mehrenberger, *P1-conservative solution interpolation on unstructured triangular meshes*, RR-6804, INRIA, Jan. 2009.

[3] C. Bernardi and R. Verfürth, *Adaptive finite element methods for elliptic equations with non-smooth coefficients*, Numer. Math., 85 (2000), pp. 579–608.

[4] P. Binev, W. Dahmen, and R. DeVore, *Adaptive finite element methods with convergence rates*, Numer. Math., 97 (2004), pp. 219–268.

[5] W. Cao, *On the error of linear interpolation and the orientation, aspect ratio, and internal angles of a triangle*, SIAM J. Numer. Anal., 43 (2005), pp. 19–40.

[6] M. J. Castro-Díaz, F. Hecht, B. Mohammadi, and O. Pironneau, *Anisotropic unstructured mesh adaptation for flow simulations*, Int. J. Numer. Meth. Fluids, 25 (1997), pp. 475–491.

[7] L. Chen, P. Sun, and J. Xu, *Optimal anisotropic simplicial meshes for minimizing interpolation errors in L^p-norm*, Math. Comp., 76 (2007), pp. 179–204.

[8] P. Clément, *Approximation by finite element functions using local regularization*, Revue Française d'Automatique, Informatique et Recherche Opérationnelle, R-2 (1975), pp. 77–84.

[9] L. Formaggia and S. Perotto, *New anisotropic a prioiri error estimate*, Numer. Math., 89 (2001), pp. 641–667.

[10] P. Frey and F. Alauzet, *Anisotropic mesh adaptation for* CFD *computations*, Comput. Meth. Appl. Mech. Engrg., 194 (2005), pp. 5068–5082.

[11] P. J. Frey, `Yams`, *a fully automatic adaptive isotropic surface remeshing procedure*, RT-0252, INRIA, nov 2001.

[12] P.-L. George, `Gamhic3d`, *a fully automatic adaptive mesh generation method in three dimensions*, Technical Note, INRIA, 2001.

[13] H. W. Carlson and R. J. Mack and O. A. Morris, *A wind-tunnel investigation of the effect of body-shape on sonic-boom pressure distributions*, TN. D-3106, Nasa, 1965.

[14] W. Huang, *Metric tensors for anisotropic mesh generation*, J. Comp. Phys., 204 (2005), pp. 633–665.

[15] J.-F. Lagüe and F. Hecht, *Optimal mesh for P_1 interpolation in H^1 semi-norm*, in Proc. of 15th Meshing Rountable, Springer, 2006, pp. 259–270.

[16] A. Loseille and F. Alauzet, *Continuous mesh framework. Part I: well-posed continuous mesh and interpolation error models*, SIAM J. Numer. Anal., (2010). Submitted.

[17] A. Loseille, A. Dervieux, and F. Alauzet, *Fully anisotropic goal-oriented mesh adaptation for 3D steady Euler equations*, J. Comp. Phys., 229 (2010), pp. 2866–2897.

[18] M. Picasso, *An anisotropic error indicator based on Zienkiewicz-Zhu error estimator: Application to elliptic and parabolic problems*, SIAM J. Sci. Comput., 24 (2003), pp. 1328–1355.

[19] O. C. Zienkiewicz and J. Z. Zhu, *The superconvergent patch recovery and a posteriori error estimates. Part 1: The recovery technique*, Int. J. Numer. Meth. Engrg., 33 (1992), pp. 1331–1364.

[20] ———, *The superconvergent patch recovery and a posteriori error estimates. Part 2: Error estimates and adaptivity*, Int. J. Numer. Meth. Engrg., 33 (1992), pp. 1365–1380.